We are IntechOpen,
the world's leading publisher of
Open Access books
Built by scientists, for scientists

6,900
Open access books available

186,000
International authors and editors

200M
Downloads

Our authors are among the

154
Countries delivered to

TOP 1%
most cited scientists

12.2%
Contributors from top 500 universities

CLARIVATE ANALYTICS
BOOK CITATION INDEX
INDEXED

WEB OF SCIENCE™

Selection of our books indexed in the Book Citation Index
in Web of Science™ Core Collection (BKCI)

Interested in publishing with us?
Contact book.department@intechopen.com

Chapter

Study on the Perspective of Mechanical Properties and Corrosion Behaviour of Stainless Steel, Plain and TMT Rebars

Indrajit Dey, Pallabi Manna, Muralidhar Yadav,
Nisith Kumar Tewary, Jayanta Kumar Saha
and Swarup Kumar Ghosh

Abstract

In the present research, the effects of various alloying elements and microstructural constituents on the mechanical properties and corrosion behaviour have been studied for four different rebars. The microstructures of stainless steel and plain rebar primarily reveal equiaxed ferrite grains and ferrite-pearlite microstructures, respectively, with no evidence of transition zone, whereas tempered martensite at the outer rim, followed by a narrow bainitic transition zone with an internal core of ferrite-pearlite, has been observed for the thermomechanically treated (TMT) rebars. The hardness profiles obtained from this study display maximum hardness at the periphery, which decreases gradually towards the centre, thereby providing the classical U-shaped hardness profile for TMT rebars. The tensile test results confirm that stainless steel rebar exhibits the highest combination of strength (≈755 MPa) and ductility (≈27%). It has been witnessed that in Tafel plots, the corrosion rate increases for all the experimental rebars in 1% HCl solution, which is well expected because the acid solutions generally possess a higher corrosive environment than seawater (3.5% NaCl) due to their acidic nature and lower pH values. However, all the experimental results obtained from Tafel and Nyquist plots correlate well for both 1% HCl and 3.5% NaCl solutions.

Keywords: stainless steel, reinforced bar, TMT, microstructure, mechanical properties, corrosion behaviour

1. Introduction

For the past few years, an inspection of reinforced concrete structures with steel rebars has become a subject of research because concrete provides an alkaline environment that is suitable for the spontaneous passivation of steel rebars. These steel rebars act as a reinforcement when tensile loads are applied [1]. But, still, there is a possibility of corrosion in these steel rebars when aggressive chloride ions are

present in the environment [1]. Corrosion in rebars may result in surrounding concrete cracking, reduction in the bond strength of the concrete and the rebars and lowering the combination of strength and ductility [1–3].

Extensive research has been carried out to date on corrosion in steel rebars but a modest solution can be the usage of stainless steels rebars as a partial or complete replacement of the reinforcements in concrete. This solution is economically viable because there may be a higher initial investment cost but this can be compensated by low-repairing cost, less maintenance effort and most importantly long-range services of the designed structures [4]. As per earlier studies, it is well established that austenitic stainless steels can be considered as the common choices for rebars, whereas there is a wide range of applications of the ferritic and the duplex stainless steels that include structural components in the construction industries [1, 5]. However, it cannot be domineered that the austenitic stainless steels are expensive due to the higher content of elements such as Ni and Mo. It has been reported earlier that stainless steel eliminates chances of corrosion but does not rely on concrete when it is subjected to the ingress of chlorides from marine environments. For the last few years, plenty of research has been carried out in search of more economically friendly novel stainless steels as reinforcements [6–12]. It is also true that, since the cost of these steels can be compared with the cost of common black steel reinforcement rather than the cost of highly alloyed stainless steels, the use of low alloyed stainless steel reinforcement has been accepted as economically more convenient [6].

Thermo-mechanical treatment (TMT) has gained researchers' attention for producing high-strength steels with lean chemistry at a reduced cost with excellent mechanical properties [13–16]. In TMT, simultaneous application of heat and deformation causes microstructural refinements [16–18]. These materials are highly used in the construction sectors for the construction of dams, bridges, buildings, flyovers and also in various other structural materials [16, 19]. The durability of these TMT rebars is an immense problem due to corrosion in reinforced concrete structures, which is needed to be minimized as much as possible to enhance the life of that structure. Substandard quality rebars can also cause damage to the towers, buildings and other constructions in the seismic zones. However, in reinforcement concrete, the presence of alkaline solution protects the TMT rebars from corrosion due to the formation of a passive layer over the steel surface [20–22]. However, encountering chloride solution in this structure causes the breakdown of this passive layer. In the coastal and marine areas, excessive level of chloride causes problems of chloride-induced corrosion, thereby creating problems in corrosion resistance of the TMT rebars in the concrete [23–27].

It is well established that corrosion of steel reinforcement bars primarily depends on the stability of different phases that are likely to form in the cement paste and the effectiveness of the oxide layer that forms on the steel bar surface, that is, the passive layer [28]. It has been reported earlier that the concrete pore solutions preserve a strongly alkaline medium due to the significant filling of calcium hydroxide in the concrete pores depending on the hydration reactions of cement. This alkaline environment is suitable for the formation of a stable passive film on the rebar surface and thereby provides significant protection to the steel rebar against corrosive environments [28]. However, chloride-induced corrosion has been reported as a primary source for the local breakdown of this passive film on the surface of the steel bars [28–30]. It is also known that the volume of rebar increases when the corroded product forms on the rebar surface and results in cracks in the concrete, thereby causing failure [27].

This paper primarily emphasizes the study of mechanical and corrosion behaviours of different types of rebars in two different aqueous solutions. It is expected that this study will provide valuable information regarding the improvement in the design parameters and also the life cycle cost calculation of various structures as well as towards the selection of the best-suited rebars for industrial and marine construction purposes.

2. Experimental procedure

Four different steel rebars such as Fe-600, galvanized steel, stainless steel and plain rebars were chosen for this study. The approximate diameters of these samples were 12 mm, 8 mm, 16 mm, and 11 mm, respectively. Notably, Fe-600 and galvanized rebars are thermomechanically treated, whereas the other two (stainless and plain) rebars were not subjected to thermomechanical treatment. The nominal chemical compositions (wt. %) of all the rebar samples are given in **Table 1**. First, the samples of suitable size were cut from these steel rebars as per the requirement of optical, hardness, tensile and corrosion tests. All the samples were then tested in an optical emission spectrometer (Thermo 3460) to analyse the chemical compositions of the rebars. Standard metallographic sample preparation techniques such as grinding (belt and paper) followed by polishing (coarse, fine and diamond) and etching by using 2% nital and Snyder solutions were used to observe the microstructural constituents under an optical microscope (Leica) and scanning electron microscope (SEM).

The etched samples were further used for the Vickers Micro-Hardness Testing (Leica-VMHT) under 300 gf load and 20 seconds dwell time to analyse micro-hardness profile throughout the cross sections with a particular interval of distance. Hardness was measured on the sample surface as a function of distance from the edge to edge, keeping an interval of 50 μm, and the recorded variation in hardness values was then plotted. It is important to mention here that the hardness profile instead of surface hardness was recorded because the hardness values were expected to decrease from the periphery to the centre. A universal testing machine (UTN-10) was utilized to conduct the tensile test with a crosshead speed of 4.5 mm/min and a gauge length of 65 mm.

The electrochemical measurements were performed using a working electrode (embedded rebar specimen); a counter electrode (graphite) was placed to one side of the rebar specimen and also an independent reference electrode; that is, saturated calomel electrode (SCE) was used to observe the corrosion behaviour. Precise electrode placement was not critical, since the conductivity of the electrolytes was high. The equipment used to observe the corrosion behaviour of the rebar samples was Origalys Potentiostat, combined with the Origamaster 5 module. Electrochemical impedance spectroscopy (EIS) was utilized in the frequency range of 100 kHz–100 MHz with an AC voltage of 5 mV. The characteristic capacitance of this frequency band was maintained in between 10^{-9} and 10^{-6} F/cm^2 [10]. The rebar samples of standard size (area) were prepared and then immersed in two different types of solution of 3.5% NaCl and 1% HCl. These particular concentrations were chosen to simulate the saline conditions possible in marine and acidic rain in industrial areas [31, 32]. In this context, it is important to mention that the area was ≈76 mm^2 for Fe 600 rebar, whereas the same for the other three samples was kept at ≈75 mm^2 for the EIS study.

3. Results and discussion

3.1 Alloy composition

Table 1 shows the compositional analysis of the different types of TMT rebars (IS 1786: 2008 for Fe 600 and IS 12594:1988 for galvanized). It has been already reported that an increase in yield strength of reinforcing bars occurs by raising carbon as well as manganese content or by microalloying. It is also true that higher carbon content may cause lower weldability and ductility [13, 16, 23]. It is worth mentioning here that all the steel rebar samples selected in the present investigation contain a lower amount of carbon since a higher amount of carbon can cause harmful carbide formation and pearlite formation in the as-rolled steels thereby causing micro-galvanic corrosion [23, 33]. Major alloying elements other than carbon are manganese and silicon in the case of all the rebar samples. However, in the case of stainless steel rebar (IS 16651:2017), apart from these two elements, chromium and nickel are also present to enhance the 'stainless' property of this steel by forming a stable and protective oxide layer to make them corrosion-resistant [34–36]. In this context, it is imperative to mention here that the corrosion resistance of the stainless steel rebar depends on the formation of the chromium layer (≈5 nm thickness) and the content of chromium that keeps the rebar surface electrochemically passive in corrosive environments [37]. It is well known that manganese increases the hardenability and tensile strength of the steel [23, 33]. The addition of silicon is beneficial to increase the hardness and strength. It also acts as a deoxidizer during the casting of the rebar, thereby helps in reducing the casting defects and allows sound steel castings [23, 38].

3.2 Microstructure analysis

3.2.1 Optical micrographs

Figure 1 shows the optical micrographs of different rebar samples (cross section). **Figures 1(a)** and **(b)** reveals the optical micrographs of the Fe 600 and galvanized rebar samples, respectively, that exhibit intermediate zones with three distinctly separate regions for both the samples. On the other hand, microstructures consisting of equiaxed ferrite grains for stainless steel (**Figure 1(c)**) and ferrite-pearlite type for plain rebar (**Figure 1(d)**) have been observed throughout the samples because these two rebars were processed through the conventional cold rolling process and not subjected to thermomechanical treatments (TMT). The presence of dark peripheral ring (edge/rim) consists of tempered martensite with an intermediate narrow transition zone of bainite with a comparably grey core with ferrite-pearlite microstructure as shown in **Figures 1(a)** and **(b)** [23, 33, 39, 40]. It is imperative to mention here that in the TMT process, quenching of hot-rolled bars

Rebar specimen	C	Mn	Si	Cr	Ni	S	P
Fe 600	0.30	0.23	0.16	—	—	0.04	0.035
Galvanized	0.22	0.58	0.23	0.03	—	0.04	0.035
Stainless steel	0.022	0.65	0.36	12.98	0.09	0.008	0.021
Plain	0.126	0.526	0.175	0.007	0.018	0.046	0.078

Table 1.
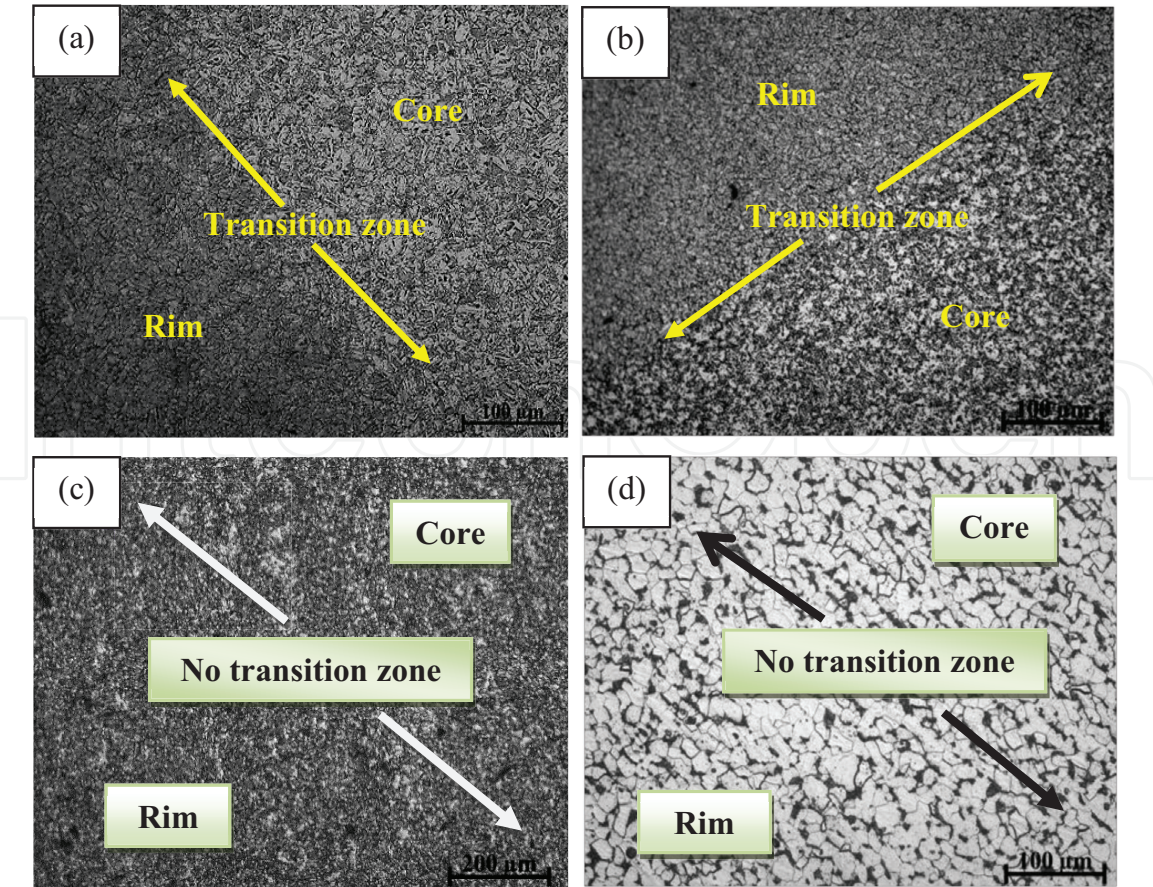*Chemical composition (wt. %) of all the experimental rebar specimens.*

Figure 1.
Optical micrographs of different rebar samples (a) Fe 600, (b) galvanized rebar, (c) stainless steel and (d) plain rebar.
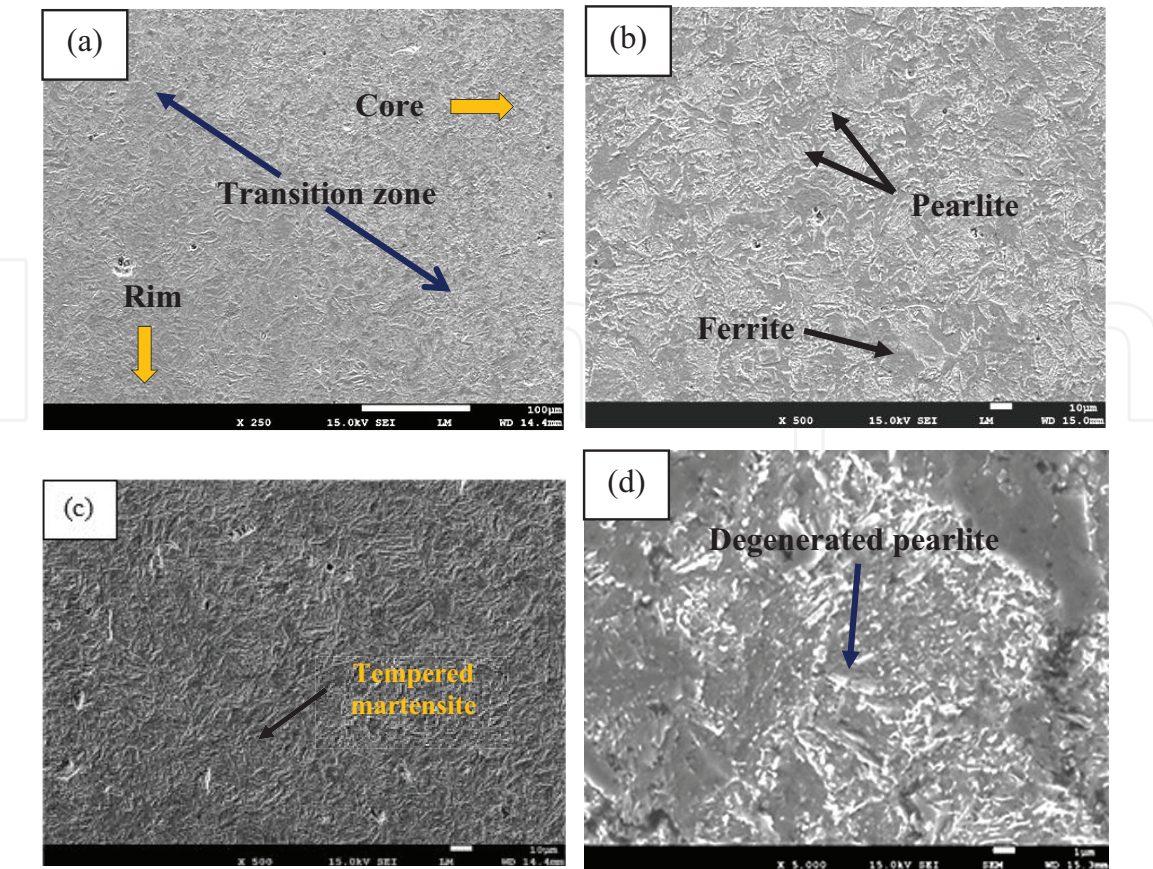

Figure 2.
SEM micrographs of Fe 600 rebar sample showing (a) transition zone, (b) core region, (c) outer rim region and (d) pearlite at higher magnification.

with water jet leads to the formation of martensite at the outer surface of the rebars. The residual heat flow across their bar section during cooling results in the tempering of the initially formed martensite with finer grains, which is self-tempering in nature and also produces ferrite-pearlite with coarser grains or mixed microstructure in the core region [13, 33, 41, 42]. A clear boundary separating the outer ring from the inner core is also visible in the case of TMT rebars (**Figures 1(a)** and **(b)**). This boundary can be considered as the demarcation line between the tempered martensite and ferrite-pearlite microstructures.

3.2.2 SEM micrographs

Figures 2 and **3** reveal the SEM microstructures of the Fe 600 rebar and galvanized rebar samples, respectively, consisting of the tempered martensitic rim at the periphery as shown in **Figures 2(c)** and **3(c)**, along with a transition zone consisting of bainite as shown in **Figures 2(a)** and **3(a)**, followed by a ferrite-pearlite mixed microstructure in the core as shown in **Figures 2(b)** and **3(b)**. In this context, it is noteworthy to mention here that the pearlite microstructure that is shown in **Figure 2(d)** reveals the presence of degenerated pearlite in the case of the Fe 600 rebar sample, which can be correlated with inadequate carbon diffusion during cooling. Detailed discussion on the formation of degenerated pearlite and bainite is available in the literature [23, 33, 39–44]. **Figure 3(d)** primarily reveals pearlite microstructure at a higher magnification with greyish ferrite and whitish cementite flake-like structures, which is completely distinguishable for galvanized rebar samples.
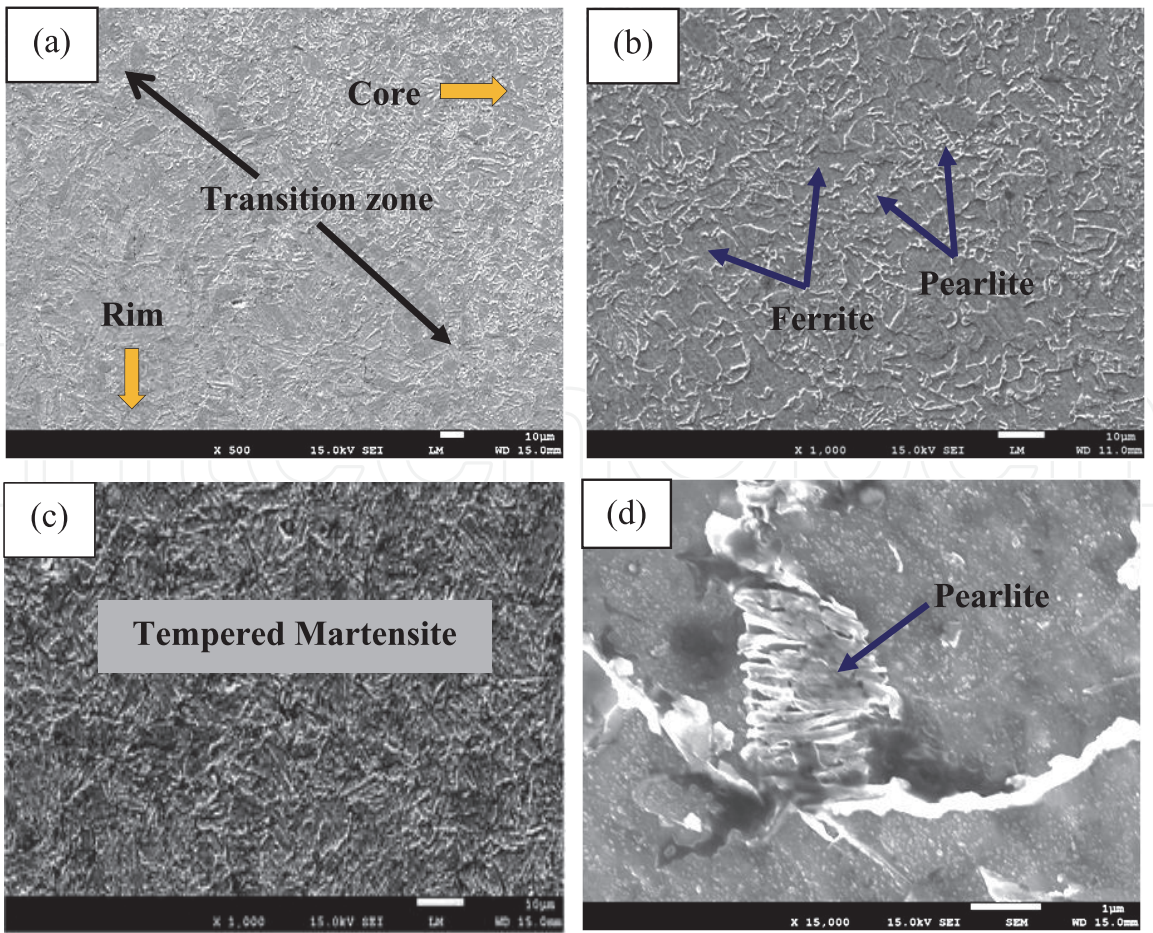

Figure 3.
SEM micrographs of galvanized rebar sample showing (a) transition zone, (b) core region, (c) outer rim region, and (d) pearlite at higher magnification.
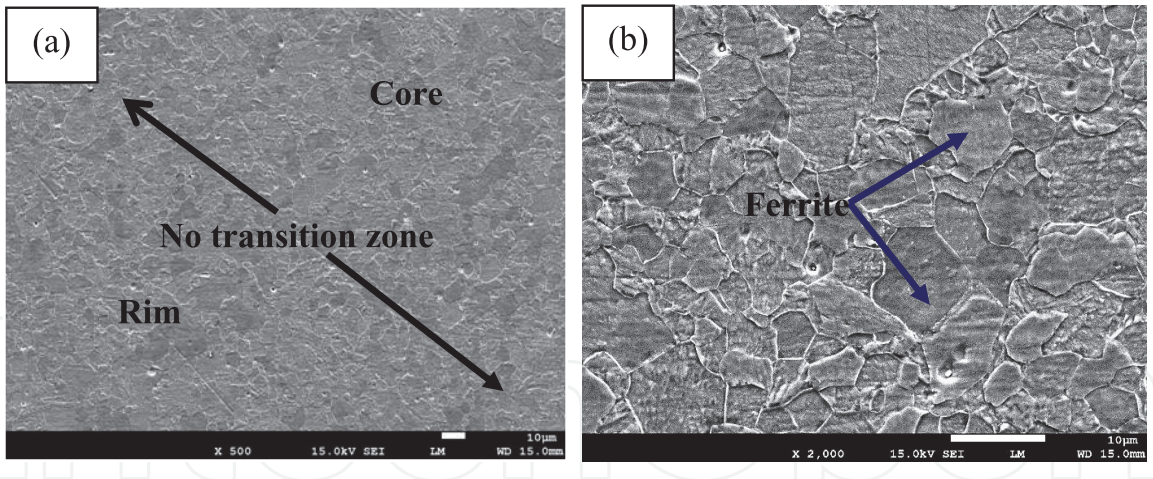
Figure 4.
SEM micrographs of stainless steel rebar sample showing (a) no transition zone and (b) higher magnification micrograph showing equiaxed ferrite grain.

SEM microstructures of stainless steel rebar and plain rebar samples are shown in **Figures 4** and **5**, respectively. These microstructures mainly consist of equiaxed grains of ferrite separated by clearly visible distinct grain boundaries in the case of stainless steel rebar sample as shown in **Figure 4(b)**. It cannot be overruled that as the carbon percentage is very low and chromium (ferrite stabilizer) percentage is high for the investigated stainless-steel rebar, hence the microstructure is ferritic. However, mixed ferrite-pearlite microstructures with no transition zone throughout the sample have been observed for plain rebar. The lamellar configuration of pearlite with some amount of resolved pearlite has been shown at a higher magnification at the inset of **Figure 5(b)**.

3.3 Mechanical properties

3.3.1 Hardness profile analysis

Figure 6 shows the hardness profiles of different types of steel rebar samples (along the cross-sectional diameter). It has been reported earlier that the hardness value of TMT rebar samples becomes maximum at the periphery due to the presence of tempered martensite, which gradually decreases towards the
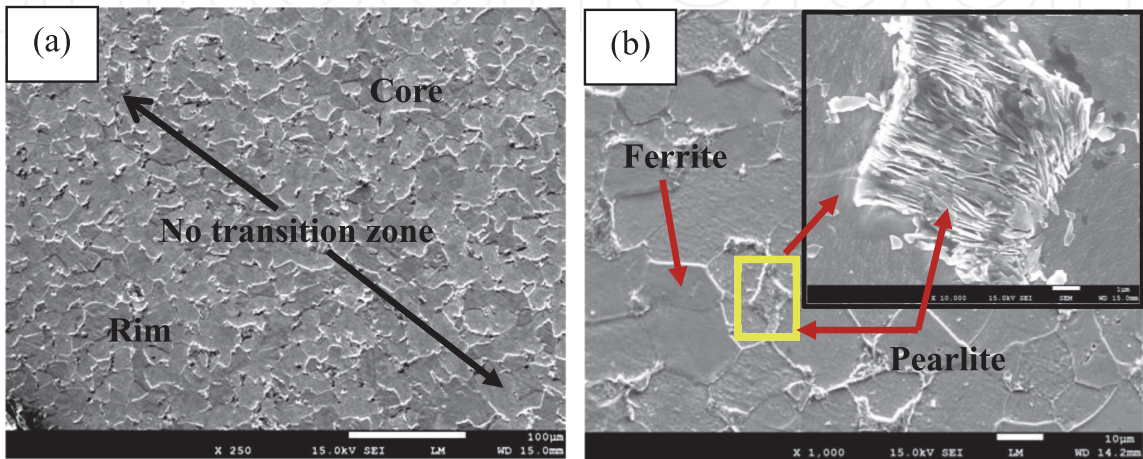

Figure 5.
SEM micrographs of plain rebar sample showing (a) no transition zone and (b) pearlite at higher magnification.

7

centre due to the formation of ferrite-pearlite mixed microstructure thereby exhibiting the classical U-shaped profiles [13, 23, 45]. It has been observed that the hardness value of Fe 600 and galvanized rebar samples in the periphery or outer rim region is around ≈285 HV, which is an indication of the presence of the tempered martensite or bainite phase [23, 45]. It has been also observed that the hardness value of the transition zone is ≈220 HV for both TMT rebar samples due to the presence of lower bainite, whereas for the core region or ferrite-pearlite region, the hardness value is ≈200 HV for Fe 600 rebar and ≈180 HV for galvanized rebar, respectively.

Figures 7(a) and **(b)** displays the comparative hardness variations for stainless steel and plain rebar samples, respectively. It is evident from **Figure** 7 that the stainless steel rebar shows higher values of hardness (≈195 HV to 260 HV) than the plain rebar (≈145 HV to 205 HV). Previous studies have confirmed that the hardness value in steel samples predominantly depends on the carbon equivalent value (CEV) [23]. It has been also reported that the weldability primarily depends on CEV for carbon steel; that is, higher CEV leads to a hard and brittle heat-affected zone (HAZ). The microstructure in the HAZ zone has an important role in the mechanical properties of the weldment; therefore, CEV is an important parameter for rebars [46]. **Table 2** summarizes the estimated carbon equivalent values of different rebar samples that were calculated by using Eq. (1). It can be seen in **Table 2** that the plain rebar sample shows the lowest CEV (≈0.2163), thereby showing the lowest value of hardness among all the samples. It is imperative to mention here that although the stainless steel rebar consists of only equiaxed ferrite microstructure (**Figure 4**), due to high carbon equivalent value and the presence of other alloying elements such as Mn, Si, Ni (**Table 1**), and it shows a higher hardness value. It cannot be domineered that Fe 600 steel rebar has a higher value of CEV (≈0.3383) than that of galvanized rebar (≈0.3227), which results in a higher core hardness value (≈196 HV) (**Figure 6**) when compared with that of galvanized rebar sample (≈184 HV). The aforesaid two TMT rebars with CEV < 0.42 according to IS 1786:2008 standard will exhibit superior weldability. However, the
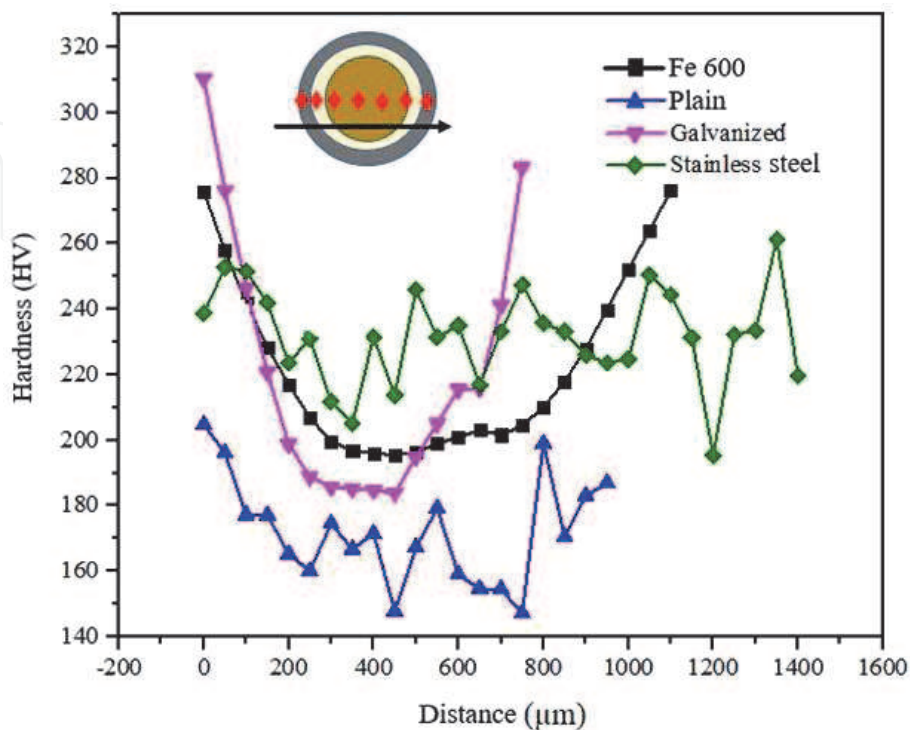

Figure 6.
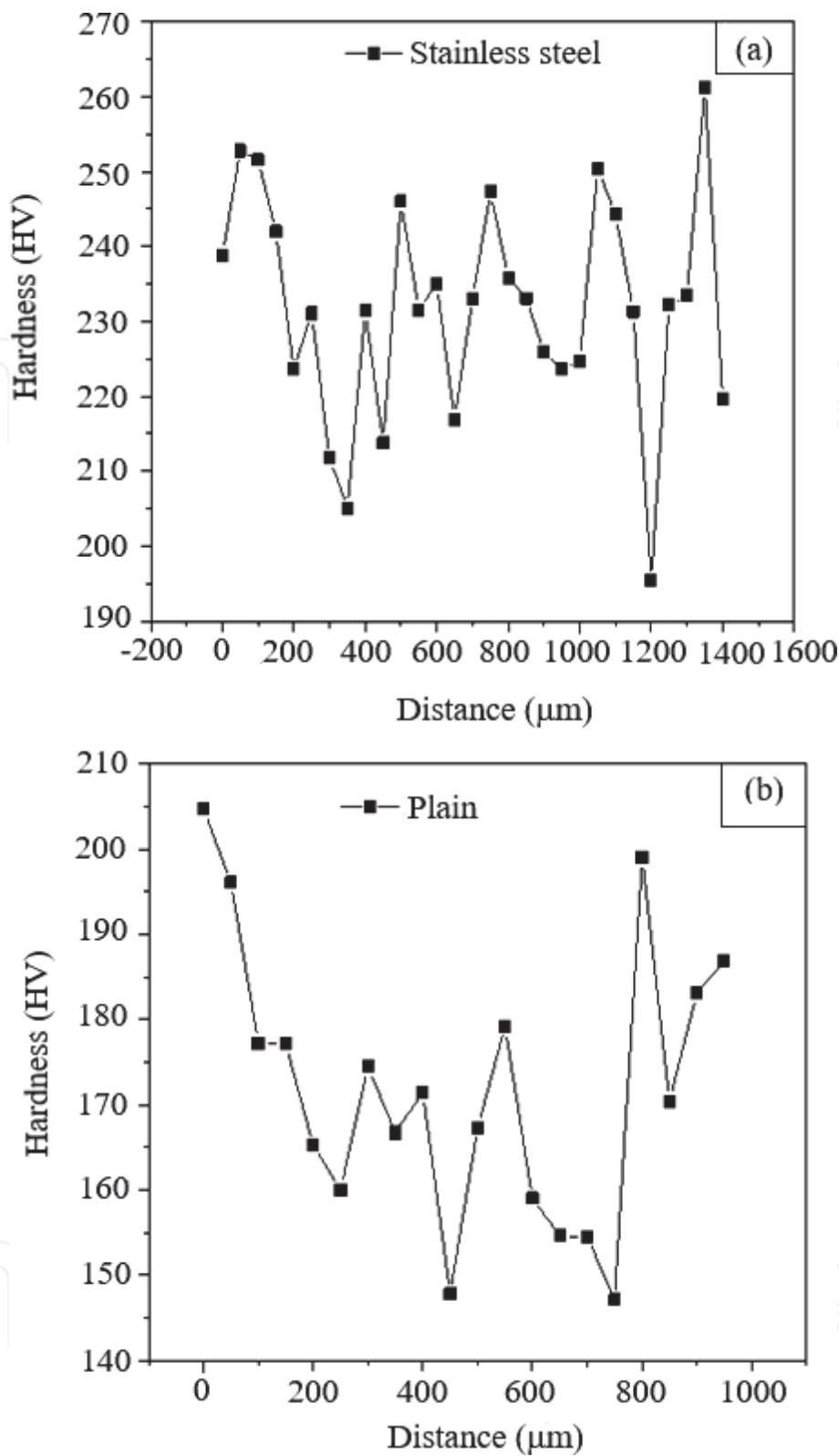*A comparison of hardness data among all the rebar specimens.*

Figure 7.
Plots showing the variation of hardness with distance for (a) stainless steel rebar and (b) plain rebar samples.

Rebar specimen	Carbon Equivalent Value (CEV)
Fe 600	0.3383
Galvanized	0.3227
Stainless steel	2.7323
Plain	0.2163

Table 2.
Estimated carbon equivalent value (CEV) for different rebar samples.

9

stainless steel rebar (ferritic grade) shows higher CEV (≈ 2.7323) because of higher Cr content but it can be welded in accordance with IS 16651:2017.

$$\text{CEV} = \text{C} + \text{Mn}/6 + \{(\text{Cr} + \text{Mo} + \text{V})/5\} + \left\{\frac{\text{Cu} + \text{Ni}}{15}\right\} \qquad (1)$$

(Where all the elemental values are expressed in wt.%)

3.3.2 Tensile properties

Table 3 summarizes the values of yield strength (YS), ultimate tensile strength (UTS), UTS/YS ratio and ductility in terms of elongation percentage (% EL) of different rebars. From **Table 3**, it is evident that the highest combination of strength and ductility has been achieved for stainless steel, followed by Fe 600 rebar among all the experimental rebars. It is a well-established fact that a higher CEV leads to higher UTS variations (**Table 2** *vis à vis* **Table 3**) [23]. **Table 4** shows the estimated ring diameter and area of tempered martensite in TMT rebars. It is noteworthy to mention that a greater amount of tempered martensitic ring area leads to higher strength (**Table 3** *vis à vis* **Table 4**) in the case of Fe 600 rebar. The estimated ring area of tempered martensite ($\approx 39.56\%$) in Fe 600 rebar results in higher strength and lower ductility compared with the galvanized rebars with $\approx 20.10\%$ ring area. It has been also noticed from **Table 4** that the area percentage of tempered martensite ring increases with the increasing diameter of the tempered martensitic rim. Plain rebar shows the maximum ductility due to the lower carbon content, whereas stainless steel with the lowest carbon and higher Cr contents having a completely ferritic microstructure and ferrite being a soft phase exhibits somewhat lower ductility than plain rebar. From earlier research, it has been observed that in seismic zones according to the ASTM A706:2006, UTS/YS ratio should be kept ≈ 1.25 [23, 33]. Previous studies have confirmed that rebars with UTS/YS ratio ≈ 1.19–1.24 provide greater advantages to their fatigue life [23, 47]. Therefore, it is clear from **Table 3** that stainless steel rebar with UTS/YS value ≈ 1.20 can become a potential candidate for the seismic hazard zone, whereas the other experimental rebars with lower values of UTS/YS ratio are expected to show better load resistance capacity in the seismic zone [23, 48].

Rebar specimen	YS (MPa)	UTS (MPa)	(UTS/YS)	Elongation (%)
Fe 600	600	660	1.10	10
Galvanized	500	545	1.09	12
Stainless steel	630	755	1.20	27
Plain	409	470	1.15	29

Table 3.
Tensile properties of various experimental rebar specimens.

Rebar specimen	Tempered martensite ring diameter (mm)	Tempered martensite ring area (%)
Fe 600	1.38	39.56
Galvanized	0.67	20.10

Table 4.
Estimated ring diameter and area of tempered martensite in TMT rebars.

3.4 Corrosion behaviour

3.4.1 Polarization curves

Figures 8 and **9** display the Tafel plots of different rebars in acid (1% HCl) and seawater (3.5% NaCl) solutions. It can be seen from **Figures 8(a)** and **(b)** that in 1% HCl solution, stainless steel rebar undergoes passivation, while other rebars show a constant enhancement of anodic current density with increasing applied potential. Generally, the state of corrosion in rebars can be classified as passive, active or
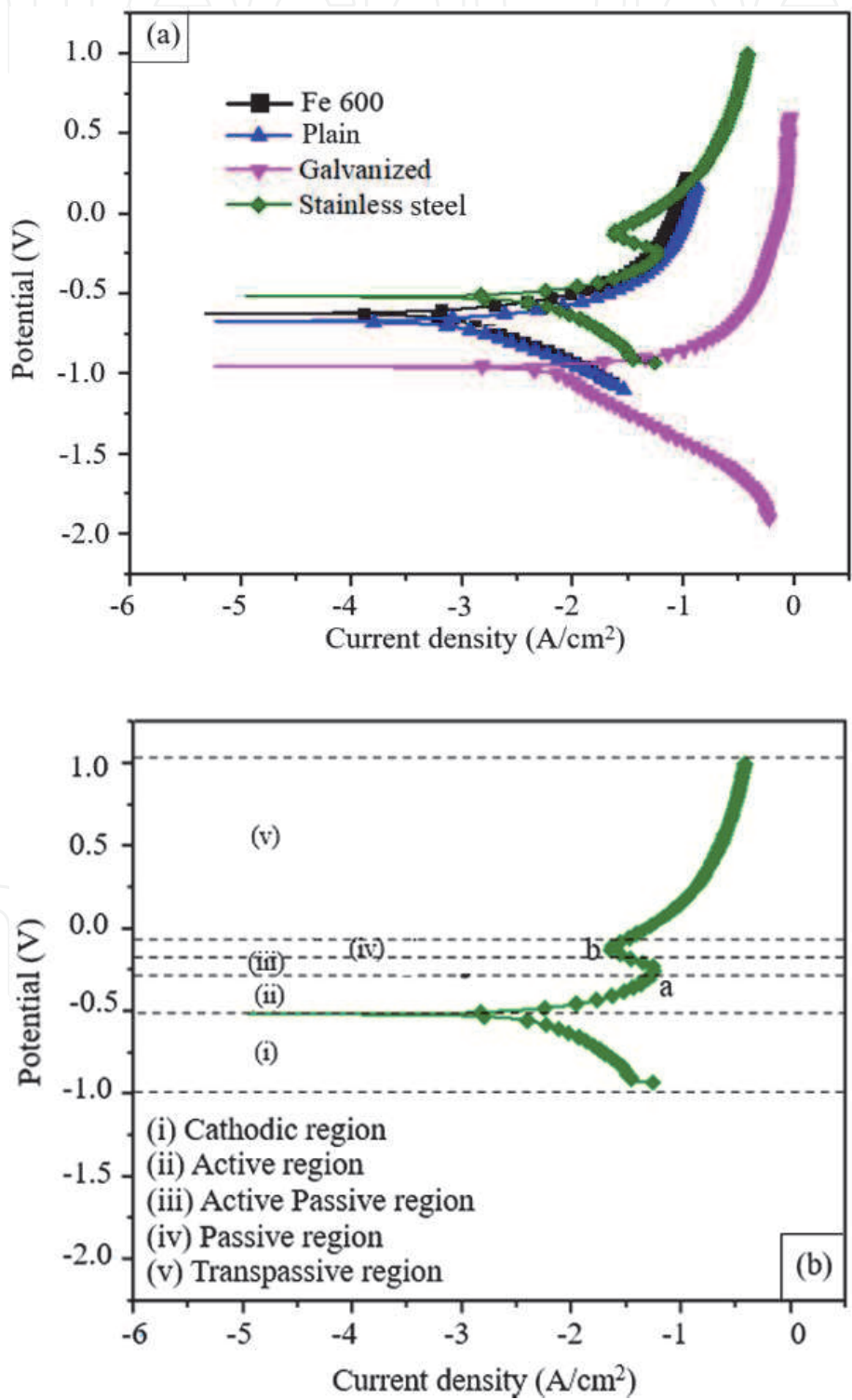

Figure 8.
(a) Tafel plots of different rebars in 1% HCl solution and (b) Tafel plot of stainless steel rebar in 1% HCl solution.
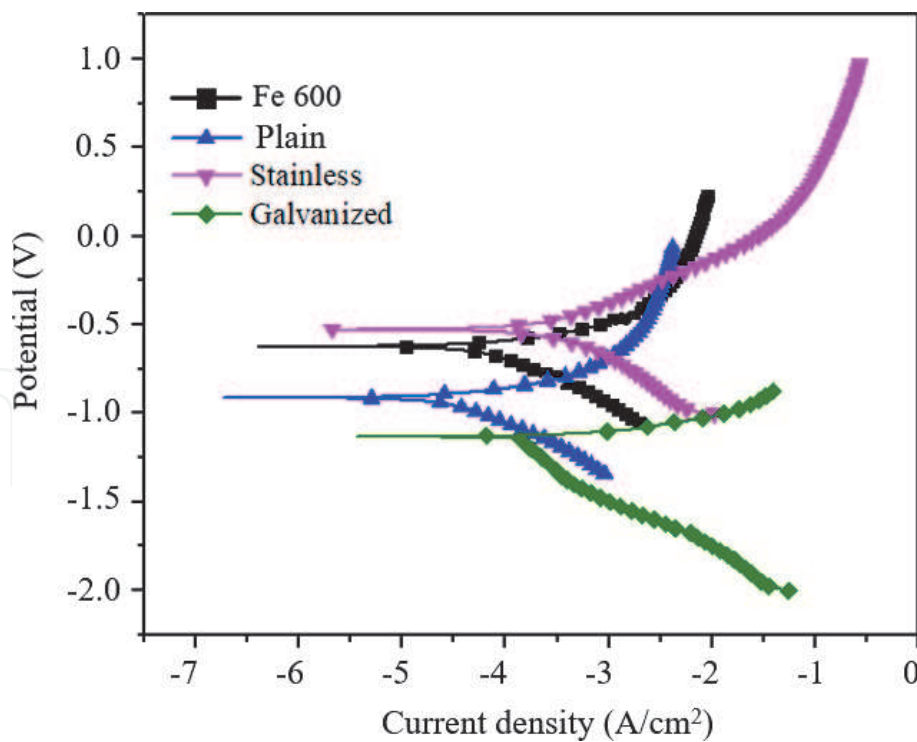
Figure 9.
Tafel plots of the rebars in 3.5% NaCl solution.

indeterminate (trans passive region), depending on the potential difference between the steel and reference electrode. **Figure 8(b)** shows that the polarization process is divided into the different zones for stainless steel at 1% HCl: (i) Cathodic region: From the corrosion potential of -0.969 V to -0.519 V, current density gradually decreases in the process. (ii) Activation region: Between -0.519 V and -0.275 V, the current density gradually increases in this region as rate of metal dissolution is higher than the rate of metal oxide formation and thereby accelerates the corrosion. (iii) Active passive region: From -0.275 V to -0.176 V, the current density starts decreasing here as the rate of metal oxide formation becomes greater than the rate of metal dissolution and metal slowly starts moving towards the passive region. (iv) Passive region: From -0.176 V to -0.058 V, metal undergoes complete passivation due to formation of chromium oxide layers and the corrosion current density becomes constant and corrosion resistance behaviour increases. (v) Trans-passive region: Above -0.058 V to 1.021 V, the passivation film is punctured due to various anodic processes, such as evolution of oxygen from water and/or the chromium oxide dissolution through Cr^{3+} to the Cr^{6+} when metal suffers high anodic polarizations; thereby, the current density increases in this region and corrosion resistance again starts decreasing. It is evident from **Figure 8(b)** that the value of current density is decreasing from point a to b, indicating greater ease of passivation by forming a stable passive film, which is similar to earlier observations [49–51]. In this connection, it is pertinent to mention here that Cr plays a major role during the transition to passive states. It has been reported earlier that increasing the Cr percentage can significantly decrease the corrosion current density values [49]. However, the analysis of the corrosion performance of different stainless steel rebars in strongly acidic environments for long-time exposure is not only limited to the effect of the elements that increase their nobility like Ni but also the effect of elements that promotes their passivation, like Cr [49]. Earlier studies have shown that the addition of both chromium and nickel to iron remarkably increases the ease of passivation [49]. It is noteworthy to mention here that when the corrosion medium changes from 1% HCl to 3.5% NaCl (**Figure 8** *vis à vis* **Figure 9**), the anodic

current density decreases as depicted by a shift of the curve along the X-axis (current density) from a value of -3 A/cm^2 to values of $((-4)$ to $(-5))$ A/cm^2 due to neutral nature of 3.5% NaCl solution and thereby showing enhanced corrosion resistance of the different types of rebars in 3.5% NaCl solution. It is evident from **Figure 9**, that the current density of Fe 600 rebar is more than the plain rebar; that is, the corrosion rate of Fe 600 rebar is greater than plain rebar. Therefore, it can be assumed from **Figures 8** and **9** that although the corrosion resistance of Fe 600 rebar is higher than plain rebar in the acid medium and it is reversed in the case of seawater. It has been also observed that the corrosion resistance of plain rebar is more than galvanized rebar because the zinc coating at the surface of galvanized rebar gets damaged due to penetration of chloride ions. In this context, it cannot be overruled that the galvanized rebar undergone through thermomechanical treatments leads to the formation of a finer rim of tempered martensite, which increases the grain boundary area, thereby leading to a higher solution attack at the grain boundary and reducing the corrosion resistance of galvanized rebars.

The corresponding polarization parameters determined by extrapolation methods from the polarization curves (**Figures 8** and **9**) are summarized in **Tables 5** and **6**. From **Table 5**, it can be seen that the corrosion potential values were more positive for Fe 600, followed by plain and stainless steel rebars in 1% HCl solution, whereas in the case of 3.5% NaCl solution, more positive corrosion potential values have been observed for stainless steel followed by plain and Fe 600 rebars as evident in **Table 6**. It is well established that the higher values of corrosion potentials lead to enhancement in the corrosion resistance properties [50, 52]. From **Tables 5** and **6**, it is noticeable that the values of i_{corr} were minimum for Fe 600 followed by plain, stainless steel and Galvanized rebars in both 1% NaCl and 3.5% HCl solutions. It is well known that higher i_{corr} values represent the higher corrosion resistance behaviour of metal. **Tables 5** and **6** also summarize the estimated values of corrosion rates that were calculated by using Eq. (2) for all the experimental rebars in both 1% HCl and 3.5% NaCl solutions. It has been observed that the

Rebars	Corrosion potential (V)	β_a (mV/dec)	β_c (mV/dec)	i_{corr} (A/cm^2)	Corrosion rate (mm/year)
Fe 600	-0.565	83.0	-279.4	0.0006219	7.225
Galvanized	-1.056	400	-2.1	0.0089603	104.09
Stainless steel	-0.588	126.9	-276.6	0.0012725	14.847
Plain	-0.572	84	-222.5	0.0007222	8.390

Table 5.
Tafel plot data of five different rebars in 1% HCl solution.

Rebars	Corrosion potential (V)	β_a (mV/dec)	β_c (mV/dec)	icorr (A/cm^2)	Corrosion rate (mm/year)
Fe 600	-0.779	356.1	-125.4	0.0000801	0.930
Galvanized	-1.131	50.3	-2438.2	0.0002522	2.929
Stainless steel	-0.527	253.3	-273.2	0.000133	1.545
Plain	-0.666	108	-262.9	0.0000744	0.864

Table 6.
Tafel plot data of five different rebars in 3.5% NaCl solution.

corrosion rate of all the experimental rebars is almost the same and very small in 3.5% NaCl as compared with 1% HCl solution. However, when the solution is 1% HCl, mm/y values obtained from **Table 5** show an increase for all the experimental rebar samples, which is well expected because the acid solutions generally possess a higher corrosive environment due to their acidic nature and pH lowering properties along with the presence of water and air, which is not seen in case of 3.5% NaCl solution due to its neutral nature [34, 53]. It is well known that a lower value of corrosion rate depicts higher corrosion resistance behaviour of the samples. According to Faraday's law, the corrosion rate can be calculated by using the corrosion current density as follows [49, 52].

$$\text{Corrosion Rate} \left(\frac{\text{mm}}{\text{year}}\right) = (3.16 \times 10^8 i_{corr} M)/(zF\rho) \qquad (2)$$

where i_{corr} is the corrosion current density in (A/cm^2), M is the molar mass of steel in (g/mol), F is the Faraday's constant (96,500 C/mol), z is the number of electrons transferred for each metal atom and ρ is the metal density (g/cm^3).where β_a = Anodic Tafel slope (mV/dec) and β_c = Cathodic Tafel slope (mV/dec).

Therefore, it is evident from these experimental results that the estimated values of corrosion rate were the lowest for Fe 600 followed by plain, stainless steel and galvanized rebars in acid solutions, but in the case of 3.5% NaCl solution, these values were significantly reduced for all the rebars, which is an indication of better corrosion resistance properties under marine environment.

3.4.2 Electrochemical impedance spectroscopy (EIS)

Figures 10 and **11** show the open-loop potential stabilities in the Nyquist plots of the experimental rebars in 1% HCl and 3.5% NaCl solutions, respectively. To compare with the results obtained from the polarization test (**Figures 8** and **9**) and also to get a better correlation, EIS studies were further performed. It is evident from
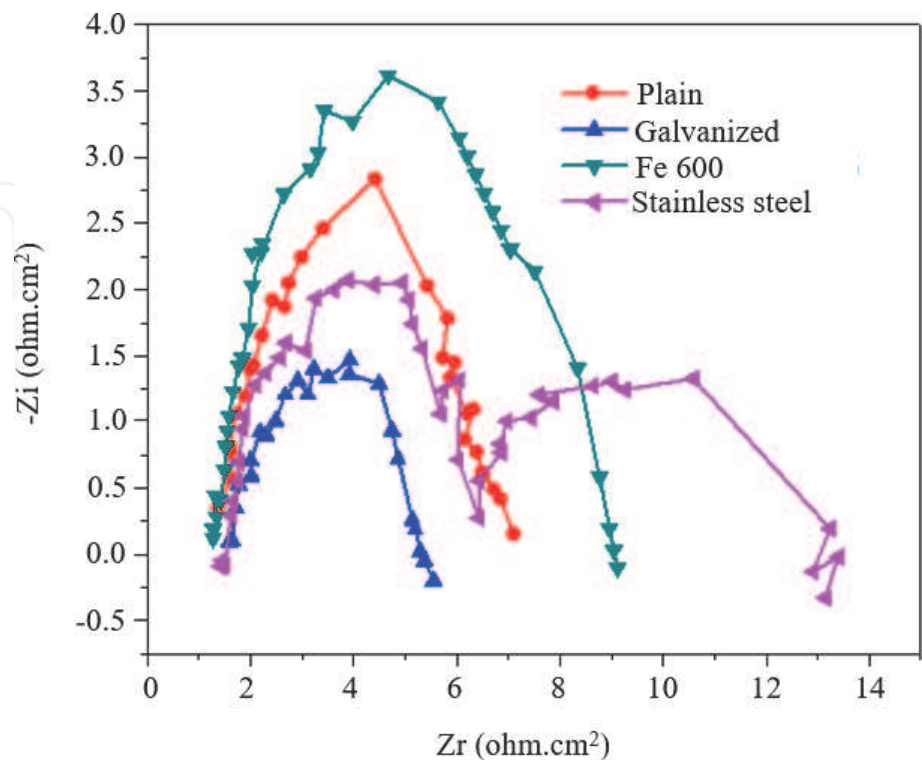

Figure 10.
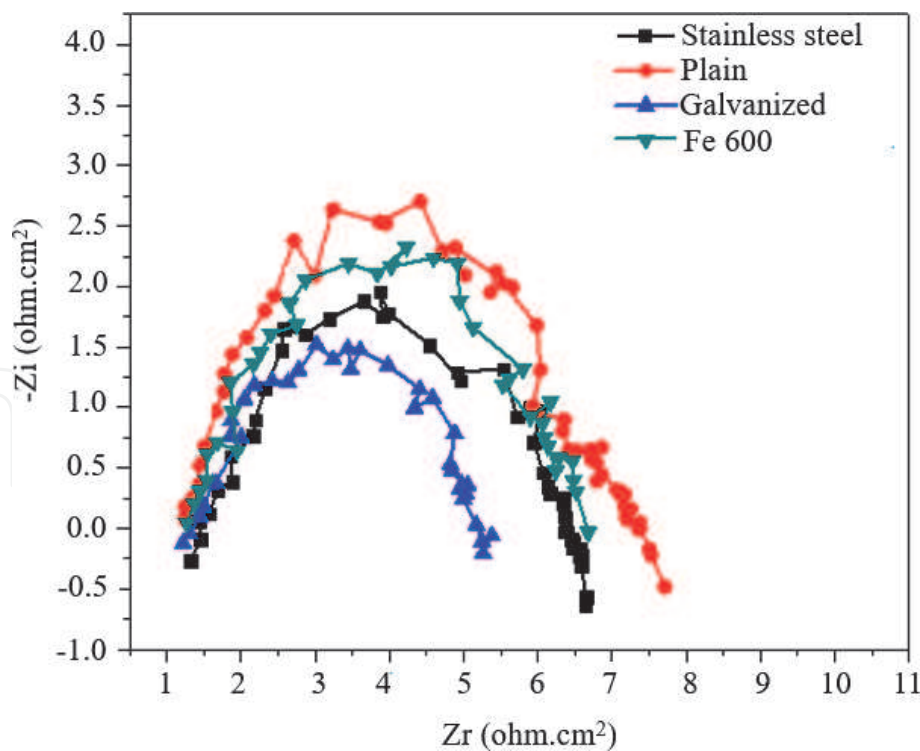*Nyquist plots of the experimental rebars in 1% HCl solution.*

Figure 11.
Nyquist plots of the rebars in 3.5% NaCl solution (seawater).

Figure 10 that except stainless steel rebar, all other rebars are showing only one semi-circular loop in the electrochemical impedance spectra, thereby indicating a capacitive semicircle in the high-medium frequency range. The occurrence of two semicircles in the electrochemical impedance spectra for stainless steel in 1% HCl is due to passivation of the rebar surface, thereby indicating a capacitive semicircle and an inductive loop in the high-medium and low-frequency ranges, respectively [52]. The capacitive semicircle represents the active state of the interface between the rebar and acid solution when the carbon steel is exposed to the corrosive solutions [52, 54]. It is well known that stainless steel will form a trans-passive zone after the damage of the passive layer, which is also evident in **Figure 8(b)**. This is due to the evolution of oxygen from water and/or the chromium oxide dissolution through Cr^{3+} to the Cr^{6+} when metal suffers high anodic polarization [49–51]. For this reason, in the Nyquist plot two loops are visible (one is bigger and the other one is smaller). However, it cannot be overruled that the open-loop diameters in **Figure 11** were maximum for the plain rebar sample, followed by Fe 600 rebar, stainless steel, and galvanized rebar. In this connection, it is noteworthy to mention here that the capacitive arcs overlap in the Nyquist plots (**Figures 10** and **11**) since concrete is a heterogeneous material and many intermixed interfacial regions influence the impedance spectra. It has been already reported that these imperfect interfaces and electrode surface roughness require a constant phase element (CPE) instead of a pure capacitor to accurately model an equivalent circuit [55].

Tables 7 and **8** summarize the values of the resistance of the electrolyte solution (R_s), the resistance of reinforced concrete (R_f) and CPE for all the rebars. It is well established that polarization resistance ($R_p = R_f + R_{ct}$) is an indicator to study the corrosion resistance behaviour of carbon steel in corrosive environments [52]. It cannot be overruled that except for stainless steel all the plots in **Figures 10** and **11** exhibit only single-loop curves for all the other rebars, which generally do not involve the charge transfer resistance (R_{ct}). Thus, the higher values of R_f reveal a higher value of corrosion resistance for the sample [52, 56]. Furthermore, the arc diameter in the Nyquist diagrams can be considered as R_f and the reduction of the

Rebar specimen	R_s (ohm.cm^2)	R_f (ohm.cm^2)	CPE ($\mu F.cm^{-2}$)
Fe 600	0.23956	13.435	105.58
Galvanized	1.6650	3.4911	2.7809
Stainless steel	2.0907	3.6110	2.8115
Plain	2.0284	10.445	30.402

Table 7.
EIS plot data of five different rebars in 1% HCl solution.

Rebar specimen	R_s (ohm.cm^2)	R_f (ohm.cm^2)	CPE ($\mu F.cm^{-2}$)
Fe 600	1.5403	4.7730	2.6929
Galvanized	1.4575	3.9449	1.5659
Stainless steel	1.8498	4.6947	2.6487
Plain	1.7141	5.5280	2.8562

Table 8.
EIS plot data of five different rebars in 3.5% NaCl solution.

arc diameter reveals a decrease in R_f values [52]. It is evident from **Table 7** that the R_f values were maximum for Fe 600, followed by plain, stainless steel, and then galvanized rebars in 1% HCl solution, whereas in 3.5% NaCl solution (**Table 8**), it is showing maximum values for plain rebar followed by Fe 600 and stainless steel rebars with a slight variation ($\approx$0.07) and then galvanized rebar, which is also in agreement with **Figures 10** and **11**. Therefore, all the experimental evidence obtained from the polarization and EIS studies under acidic and seawater solutions are in good agreement and the corrosion resistance of all the experimental rebars is higher in 3.5% NaCl than 1% HCl solutions.

4. Conclusions

The important conclusions drawn from this study are as follows:

1. Microstructures of all the TMT rebars consist of an outer martensitic rim with an intermediate narrow bainitic transition zone followed by a ferrite-pearlite inner core, whereas stainless steel and plain rebars show equiaxed ferrite grain and ferrite-pearlite microstructure throughout the sample with no transition zone between core and rim due to the absence of TMT.

2. Fe 600 and galvanized rebars exhibit classical U-shaped hardness profiles, whereas stainless steel and plain rebars reveal a different variation at the edges when compared with other rebars and the absence of the classical U-shaped hardness profiles.

3. Stainless steel rebar shows the highest combination of strength ($\approx$755 MPa) and ductility (27%) among all the rebars followed by Fe 600 rebar ($\approx$660 MPa) in terms of strength. Plain rebar although showing lower values of strength ($\approx$470 MPa) shows the maximum amount of ductility ($\approx$29%). Therefore, it is expected that all the experimental rebars will show improved performance in the seismic zones.

4. In the Tafel plot and Nyquist plot, stainless steel shows a different property in 1% HCl solution than the others. This is due to the formation of the transpassive zone *via* the evolution of oxygen from water and/or the chromium oxide dissolution through Cr^{3+} to the Cr^{6+} when metal suffers high anodic polarization.

5. In the Nyquist plot, a higher R_p value indicates higher corrosion resistance. Also, the larger the radius of the capacitive loop, the greater will be the charge transfer resistance, that is, corrosion resistance. It is also true that greater current density (i_{corr}) signifies a higher corrosion rate in the Tafel plot. Therefore, it can be concluded that in both Tafel and Nyquist studies, Fe 600 rebar has revealed maximum corrosion resistance followed by plain, stainless steel and galvanized rebars in 1% HCl solution, whereas in 3.5% NaCl solution, plain rebar has shown maximum corrosion resistance and then followed by Fe 600 and stainless steel rebars with a minor variation and then galvanized rebar.

Acknowledgements

Author details

Indrajit Dey[1], Pallabi Manna[1], Muralidhar Yadav[1], Nisith Kumar Tewary[1], Jayanta Kumar Saha[2] and Swarup Kumar Ghosh[1*]

1 Department of Metallurgy and Materials Engineering, Indian Institute of Engineering Science and Technology, Shibpur, Howrah, West Bengal, India

2 Institute for Steel Development and Growth, Kolkata, West Bengal, India

*Address all correspondence to: skghosh@metal.iiests.ac.in

IntechOpen

References

[1] Li X, Lo KH, Kwok CT, Sun YF, Lai KK. Post-fire mechanical and corrosion properties of duplex stainless steel: Comparison with ordinary reinforcing-bar steel. Construction and Building Materials. 2018;**174**:150-158. DOI: 10.1016/j.conbuildmat.2018.04.110

[2] Coccia S, Imperatore S, Rinaldi Z. Influence of corrosion on the bond strength of steel rebars in concrete. Materials and Structures. 2016;**49**:537-551. DOI: 10.1617/s11527-014-0518-x

[3] Apostolopoulos CA, Papadakis VG. Consequences of steel corrosion on the ductility properties of reinforcement bar. Construction and Building Materials. 2008;**22**(12):2316-2324. DOI: 10.1016/j.conbuildmat.2007.10.006

[4] Tae SH, Kyung JW, Ujiro T, Shin SW. Service life estimation of reinforced concrete structures made using Cr-bearing rebars in microcell corrosion environments. ISIJ International. 2007;**47**(9):1315-1323. DOI: 10.2355/isijinternational.47.1315

[5] Baddoo NR. Stainless steel in construction: A review of research, applications, challenges and opportunities. Journal of Constructional Steel Research. 2008;**64**(11):1199-1206. DOI: 10.1016/j.jcsr.2008.07.011

[6] Serdar M, Zulj LV, Bjegovic D. Long-term corrosion behaviour of stainless reinforcing steel in mortar exposed to chloride environment. Corrosion Science. 2013;**69**:149-157. DOI: 10.1016/j.corsci.2012.11.035

[7] Moser RD, Singh PM, Kahn LF, Kurtis KE. Chloride-induced corrosion resistance of high-strength stainless steels in simulated alkaline and carbonated concrete pore solutions. Corrosion Science. 2012;**57**:241-253. DOI: 10.1016/j.corsci.2011.12.012

[8] Alvarez SM, Bautista A, Velasco F. Corrosion behaviour of corrugated lean duplex stainless steels in simulated concrete pore solutions. Corrosion Science. 2011;**53**:1748-1755. DOI: 10.1016/j.corsci.2011.01.050

[9] Bautista A, Blanco G, Velasco F, Gutierrez A, Soriano L, Palomares FJ, et al. Changes in the passive layer of corrugated austenitic stainless steel of low nickel content due to exposure to simulated pore solutions. Corrosion Science. 2009;**51**:785-792. DOI: 10.1016/j.corsci.2009.01.012

[10] Blanco G, Bautista A, Takenouti H. EIS study of passivation of austenitic and duplex stainless steels reinforcements in simulated pore solutions. Cement and Concrete Composites. 2006;**28**:212-219. DOI: 0.1016/j.cemconcomp.2006.01.01

[11] Luo H, Dong CF, Li XG, Xiao K. The electrochemical behaviour of 2205duplex stainless steel in alkaline solutions with different pH in the presence of chloride. Electrochimica Acta. 2012;**64**:211-220. DOI: 10.1016/j.electacta.2012.01.025

[12] Freire L, Catarino MA, Godinho MI, Ferreira MJ, Ferreira MGS, Simoes AMP, et al. Electrochemical and analytical investigation of passive films formed on stainless steels in alkaline media. Cement and Concrete Composites. 2012;**34**:1075-1081. DOI: 10.1016/j.cemconcomp.2012.06.002

[13] Paul SK, Rana PK, Das D, Chandra S, Kundu S. High and low cycle fatigue performance comparison between micro alloyed and TMT rebar. Construction and Building Materials. 2014;**54**:170-179. DOI: 10.1016/j.conbuildmat.2013.12.061

[14] Rasouli D, Khameneh S, Akbarzadeh A, Daneshi GH. Effect of

cooling rate on the microstructure and mechanical properties of micro alloyed forging steel. Journal of Materials Processing Technology. 2008;**206**: 92-98. DOI: 10.1016/j.jmatprotec. 2007.12.006

[15] Opiela M. Thermo-mechanical treatment of the C-Mn steel with Nb, Ti, V and microadditions. Archives of Materials Science and Engineering. 2007;**28**(6):377-380

[16] Ghosh A, Ghosh M. Tensile and impact behaviour of thermo mechanically treated and micro-alloyed medium carbon steel bar. Construction and Building Materials. 2018;**192**: 657-670. DOI: 10.1016/j.conbuildmat. 2018.10.098

[17] Ceschini L, Marconi A, Martini C, Morri A, Schino ADI. Tensile and impact behaviour of a microalloyed medium carbon steel: Effect of the cooling condition and corresponding microstructure. Materials and Design. 2013;**45**:171-178. DOI: 10.1016/j. matdes.2012.08.063

[18] Khan MR, Khan MM. Comparative study of the micro-structure of quenched self-tempered and ordinary steel. Journal of Pakistan Materials Society. 2008;**2**(2):82-86

[19] Rocha M, Michel S, Bruhwiler E, Nussbaumer A. Very high cycle fatigue tests of quenched and self-tempered steel reinforcement bars. Materials and Structures. 2016;**49**:1723-1732. DOI: 10.1617/s11527-015-0607-5

[20] Bertolini L, Elsener B, Pedeferri P, Redaelli E, Polder RB. Corrosion of Steel in Concrete: Prevention, Diagnosis, Repair. 2nd ed. Weinheim: Wiley-VCH; 2013

[21] Venkatesan P, Palaniswamy N, Rajagopal K. Corrosion performance of coated reinforcing bars embedded in concrete and exposed to natural marine environment. Progress in Organic Coatings. 2006;**56**:8-12. DOI: 10.1016/j. porgcoat.2006.01.011

[22] Erdogdu S, Bremner TW, Kondratova IL. Accelerated testing of plain and epoxy-coated reinforcement in simulated seawater and chloride solutions. Cement and Concrete Research. 2001;**31**:861-867

[23] Nandi SK, Tewary NK, Saha JK, Ghosh SK. Microstructure, mechanical properties and corrosion performance of a few TMT rebars. Corrosion Engineering Science and Technology. 2016;**51**(7):476-488. DOI: 10.1080/ 1478422X.2016.1141744

[24] Yu L, Francois R, Dang VH, L'Hostis V, Gagne R. Development of chloride-induced corrosion in pre-cracked RC beams under sustained loading: Effect of load-induced cracks, concrete cover, and exposure conditions. Cement and Concrete Research. 2015;**67**: 246-258. DOI: 10.1016/j.cemconres. 2014.10.007

[25] Apostolopoulos CA, Demis S, Papadakis VG. Chloride induced corrosion of steel reinforcement-mechanical performance and pit depth analysis. Construction and Building Materials. 2013;**38**:139-146. DOI: 10.1016/j.conbuildmat.2012.07.087

[26] Ye CQ, Hu RG, Dong SG, Zhang XJ, Hou RQ, Du RG, et al. EIS analysis on chloride-induced corrosion behaviour of reinforcement steel in simulated carbonated concrete pore solutions. Journal of Electroanalytical Chemistry. 2013;**688**:275-281. DOI: 10.1016/j.jele chem.2012.09.012

[27] Song HW, Saraswathy V, Muralidharan S, Lee CH, Thangavel K. Corrosion performance of steel in composite concrete system admixed with chloride and various alkaline nitrites. Corrosion Engineering Science and Technology. 2009;**44**(6):408-415. DOI: 10.1179/174327809X397848

[28] Rivera-CorraL JO, Fajardo G, Arliguie G, Orozco-Cruz R, Deby F, Valdez P. Corrosion behavior of steel reinforcement bars embedded in concrete exposed to chlorides: Effect of surface finish. Construction and Building Materials. 2017;**147**:815-826. DOI: 10.1016/j.conbuildmat.2017.04.186

[29] Dong SG, Zhao B, Lin CJ, Du RG, Hu RG, Zhang GX. Corrosion behavior of epoxy/zinc duplex coated rebar embedded in concrete in ocean environment. Construction and Building Materials. 2012;**28**:72-78. DOI: 10.1016/j.conbuildmat.2011.08.026

[30] Kar AK. Rebars for Durable Concrete Construction: Points to Ponder. Design of Cities and Buildings-Sustainability and Resilience in the Built Environment. London: IntechOpen; 2021. pp. 13-35

[31] Kamimura T, Hara S, Miyuki H, Yamashita M, Uchida H. Composition and protective ability of rust layers formed on weathering steel exposed to various environments. Corrosion Science. 2006;**48**:2799-2812. DOI: 10.1016/j.corsci.2005.10.004

[32] Loto CA, Loto RT. Electrochemical corrosion resistance evaluation of ferritic stainless steel in HCl. International Journal of Electrochemical Science. 2012;**7**:11011-11022

[33] Panigrahi BK, Srikanth S, Sahoo G. Effect of alloying elements on tensile properties, microstructure, and corrosion resistance of reinforcing bar steel. Journal of Materials Engineering and Performance. 2009;**18**:1102-1108. DOI: 10.1007/s11665-008-9336-z

[34] Tewary NK, Kundu A, Nandi R, Saha JK, Ghosh SK. Microstructural characterization and corrosion performance of old railway girder bridge steel and modern weathering

structural steel. Corrosion Science. 2016;**113**:57-63. DOI: 10.1016/j.corsci.2016.10.004

[35] Wu Z, Troparevsky MC, Gao YF, Morris JR, Stocks GM, Bei H. Phase stability, physical properties and strengthening mechanisms of concentrated solid solution alloys. Current Opinion in Solid State and Materials Science. 2017;**21**:267-284. DOI: 10.1016/j.cossms.2017.07.001

[36] Hasan MA, Yan K, Lim S, Akiyama M, Frangopol DM. LCC-based identification of geographical locations suitable for using stainless steel rebars in reinforced concrete girder bridges. Structure and Infrastructure. Engineering. 2020;**16**:1-27. DOI: 10. 1080/15732479.2019.1703758

[37] Vlack LHV. Elements of Material Science and Engineering. Vol. 4. Massachusetts: Adison-Wesley Reading; 1987. pp. 31-32

[38] Song HW, Saraswathy V. Corrosion monitoring of reinforced concrete structures–a review. International Journal of Electrochemical Science. 2007;**2**:1-28

[39] Panigrahi BK, Jain SK. Impact performance of high strength low alloy TMT reinforcement ribbed bar. Bulletin of Materials Science. 2002;**25**(4): 319-324

[40] Batusia A, Pomares JC, Gonzalez MN, Velasco F. Influence of the microstructure of TMT reinforcing bars on their corrosion behaviour in concrete with chlorides. Construction and Building Materials. 2019;**229**: 116899. DOI: 10.1016/j.conbuildmat. 2019.116899

[41] Paul SK, Majumdar S, Kundu S. Low cycle fatigue behavior of thermo-mechanically treated Rebar. Materials

and Design. 2014;**58**:402-411.
DOI: 10.1016/j.matdes.2014.01.079

[42] Khalifa H, Megahed GM, Hamouda RM, Taha MA. Experimental investigation and simulation of structure and tensile properties of Tempcore treated rebar. Journal of Materials Processing Technology. 2016;**230**: 244-253. DOI: 10.1016/j.jmatprotec. 2015.11.023

[43] Sk MB, Khan AK, Lenka S, Syed B, Chakraborty J, Chakrabarti D, et al. Effect of microstructure and texture on the impact transition behaviour of thermo-mechanically treated reinforcement steel bars. Materials and Design. 2016;**90**:1136-1150. DOI: 10.1016/j.matdes.2015.11.053

[44] Ahmed E, Ibrahim S, Galal M, Elnekhaily SN, Allam T. Microstructure and mechanical properties of V-alloyed rebars subjected to Tempcore process. Metals. 2021;**11**(246):1-17. DOI: 10.3390/met11020246

[45] Osarolube E, Owate IO, Oforka NC. Corrosion behaviour of mild and high carbon steels in various acidic medium. Scientific Research and Essay. 2008; **3**(6):224-228

[46] Odebiyi OS, Adedayo SM, Tunji LA, Onuorah MO. A review of weldability of carbon steel in arc-based welding processes. Cogent Engineering. 2019; **6**(1):1609180. DOI: 10.1080/ 23311916.2019.1609180

[47] Rajkumar C. Increasing the Yield Strength of Niobium Microalloyed Reinforcing Bar. Research Report (master of science). Johannesburg: University of Witwatersrand; 2008. pp. 14-90

[48] Zou G, Shi W, Xiang S, Ji X, Ma G, Ballinger RG. Corrosion behavior of 904L austenitic stainless steel in hydrofluoric acid. The Royal Society of

Chemistry Advances. 2018;**8**:2811-2817. DOI: 10.1039/C7RA12453H

[49] Bellezze T, Giuliani G, Roventi G. Study of stainless steels corrosion in strong acid mixture. Part 1: Cyclic potentiodynamic polarization curves examined by means of analytical method. Corrosion Science. 2018;**130**: 113-125. DOI: 10.1016/j. corsci.2017.10.012

[50] Luo H, Su H, Dong C, Xiao K, Li X. Electrochemical and passivation behavior investigation of ferritic stainless steel in simulated concrete pore media. Data in Brief. 2015;**5**:171-178. DOI: 10.1016/j.dib.2015.08.016

[51] Invernizzi AJ, Sivieri E, Trasatti SP. Corrosion behaviour of duplex stainless steels in organic acid aqueous solutions. Materials Science and Engineering A. 2008;**485**:234-242. DOI: 10.1016/j. msea.2007.08.036

[52] Zhou H, Wang Y, Ma T. Effect of silicon addition on corrosion behaviour of carbon steel rebar in sulphuric acid environment. International Journal of Electrochemical Science. 2020;**15**: 3003-3012. DOI: 10.20964/2020.04.22

[53] Bar HN, Sivaprasad S, Narasaiah N, Paul SK, Sen BN, Chandra S. Low cycle and ratchetting fatigue behaviour of high UTS/ YS ratio reinforcing steel bars. Journal of Materials Engineering and Performance. 2013;**22**:1701-1707. DOI: 10.1007/s11665-013-0470-x

[54] Husairi F, Rouhi J, Eswar K, Zainurul AZ, Rusop M, Abdullah S. Electrochemical impedance spectroscopy analysis of porous silicon prepared by photo-electrochemical etching: Current density effect. Applied Physics A. 2014;**116**:2119-2124. DOI: 10.1007/s00339-014-8416-1

[55] Sohail MG, Kahraman R, Alnuaimi NA, Gencturk B, Alnahhal W,

Dawood M, et al. Electrochemical behavior of mild and corrosion resistant concrete reinforcing steel. Construction and Building Materials. 2020;**232**: 117205. DOI: 10.1016/j.conbuildmat. 2019.117205

[56] Rouhi J, Mahmud S, Hutagalung SD, Kakooei S. Journal of Micro/ Nanolithography, MEMS, and MOEMS. 2011;**10**:043002. DOI: 10.1117/1.3643480